



Asymmetric deformation characteristics and mechanical behavior for tunnels in soft-hard inclined contact strata under high geo-stress: a case study

Hao Kou¹ · Chuan He¹ · Wenbo Yang¹ · Fangyin Wu¹ · Zihan Zhou¹ · Wei Meng¹ · Longge Xiao²

Received: 7 October 2021 / Accepted: 16 June 2022 / Published online: 28 June 2022
© Springer-Verlag GmbH Germany, part of Springer Nature 2022

Abstract

The problem of large deformation for soft rock has always been difficult in tunnel construction under high geo-stress. Previous studies have mainly focused on the single stratum, while the soft-hard contact stratum is often encountered after tunnel excavation. There are limited studies on the large deformation caused by tunnels in soft-hard inclined contact strata. This paper investigated a case on asymmetric deformation of surrounding rock and unequal pressure behavior of supporting structure in Dongmachang I tunnel at the Chenghai active fault zone. Through the in-situ stress test and three-dimensional transformation calculation, we found that the tunnel site area was dominated by horizontal stress and was in extremely high geo-stress. Besides, the analysis of field monitoring and numerical simulation pointed out that maximum squeezing deformation and pressure occurred at the left spandrel of the tunnel, and the asymmetric deformation disaster of surrounding rock and the asymmetric compression failure of secondary lining were caused by dolomitic broken limestone in soft and hard inclined contact and high geo-stress. Notably, the minimum safety factor at the left spandrel was only 0.7, which clearly showed that the secondary lining had been in a failed state. Consistent with the actual damage result, this study vividly represents the damage to the secondary lining under the biased pressure on site.

Keywords Inclined contact strata · High geo-stress · Asymmetric deformation · Mechanical behavior · Biased pressure

Introduction

Due to the continuous uplift of the Tibetan Plateau plate, the southwest region of China is characterized by large rises and falls, strong topographic cutting, and extremely strong geological structures. There were many challenges to the construction of traffic tunnels in this region, such as high geo-stress, high earthquake intensity, high geological disaster risk, crossing the broken soft rock, and active fault zone (Chen et al. 2020b). Many scholars' research results show that high geo-stress and poor rock mass quality are the main reasons for the large deformation of the tunnel (Cao et al.

2018; Meng et al. 2013; Sun et al. 2021; Tao et al. 2020). The phenomenon of asymmetric deformation also occurs in tunnel construction, and the main reason is often caused by the inclined contact of soft-hard rock or the oblique distribution of rock bedding (Chen et al. 2019a; Xu et al. 2020; Yang et al. 2018). Therefore, it is of great guiding significance to study the asymmetric deformation and mechanical behavior of tunnels in soft-hard contact strata under high geo-stress for tunnel excavation and support design.

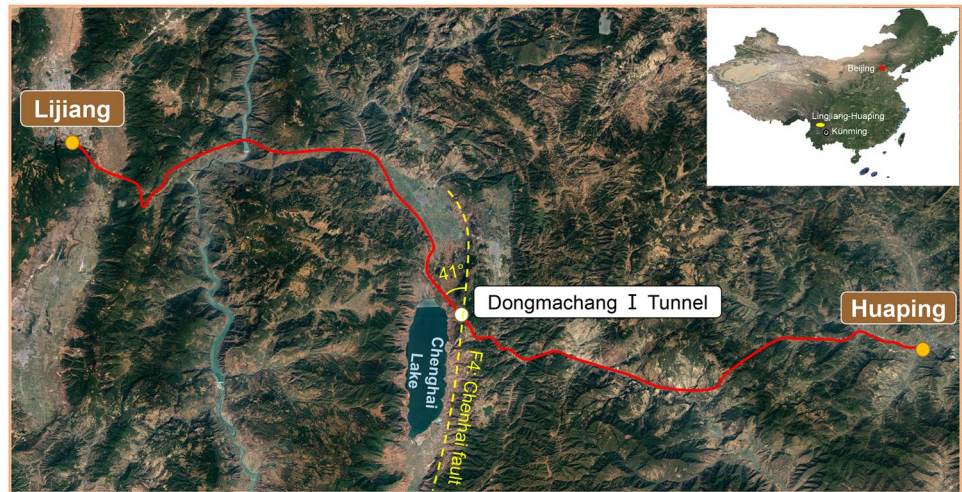
There have been some studies on the mechanical properties of soft-hard contact strata and the deformation and failure characteristics of the tunnel passing through the strata. According to rock strength and acoustic emission signal, soft and hard contact rock showed different properties from pure rock (Bai et al. 2019; Wu and Huang 2020; Yang et al. 2019a). The overall strength and acoustic emission energy were greatly influenced by the soft rock, and the strength is mainly determined by the soft rock and decreased with the increase of the soft and hard thickness ratio. The difference in surrounding rock affects the excavation method of the tunnel. For the shallow tunnel with upper-soft and

✉ Wenbo Yang
yangwenbo1179@hotmail.com

¹ Key Laboratory of Transportation Tunnel Engineering, Ministry of Education, Southwest Jiaotong University, Chengdu 610031, Sichuan, China

² China State Construction Engineering Corporation Co., Ltd., Beijing 100037, China

Fig. 1 Route map of Huaping-Lijiang highway



lower-hard stratum, Wang et al. (2019) analyzed the conversion opportunity of two excavation methods: the central diaphragm method and the bench method. Zhang et al. (2020) also explained that when the surrounding rock changed from strongly weathered conglomerate to soft soil, the wrong excavation method was the main reason for the instability of the tunnel and the large surface settlement. With the increase of the proportion of hard layer, the surface settlement decreases and the trough width increases, which is roughly linear (Ding et al. 2021). In the soft-hard contact composite stratum, it was generally the soft stratum that led to the difference in surrounding rock mechanical behavior (Shi et al. 2021). Feng et al. (2012) counted the phenomena of squeezing failure in the construction of the deep-buried and high geo-stress tunnels and found that the soft-hard contact area was the most serious, the plastic deformation range of soft rock was wider, and the strength of soft rock was much lower than that of hard rock, resulting in “higher in-situ stress” effect in soft rock. Yang et al. (2021) discussed four cases of the soft-hard contact stratum in the Jiayuan tunnel and showed that the surrounding rock pressure of the supporting structure under the contact zone is greater than that of the general stratum. Liu et al. (2021) and Chen et al. (2020a) have studied the deformation characteristics and failure mechanism of the tunnel excavated by monoclinic soft and hard interbedded rock mass. The tunnel deformation was obviously asymmetric, and the maximum deformation occurred in the normal direction of the bedding plane. The failure modes of surrounding rock mainly included four types: fracture failure, overturning failure, bending failure, shear slip failure, and buckling failure. Yang et al. (2019b) also revealed the phenomenon of asymmetric deformation and failure in soft-hard contact rock through model experiment. Therefore, we should pay more attention to the excavation and support of the complex rock tunnel, especially the

large deformation in soft layer. Most of the above studies are shallow-buried tunnels or tunnels with horizontal distribution of soft-hard rock. The asymmetric deformation and failure mechanism of soft-hard inclined contact rock tunnel under high geo-stress is still unclear, and the mechanical behavior characteristics of supporting structure need to be further studied.

In this paper, the in-situ stress distribution of tunnel cross-section was obtained by field geo-stress measurement and calculation. Based on field measurements and numerical simulation of supporting structure, the asymmetric deformation characteristic and mechanical behavior of Dongmachang I tunnel in soft-hard rock inclined contact stratum were studied, and the mechanism of tunnel disease was analyzed.

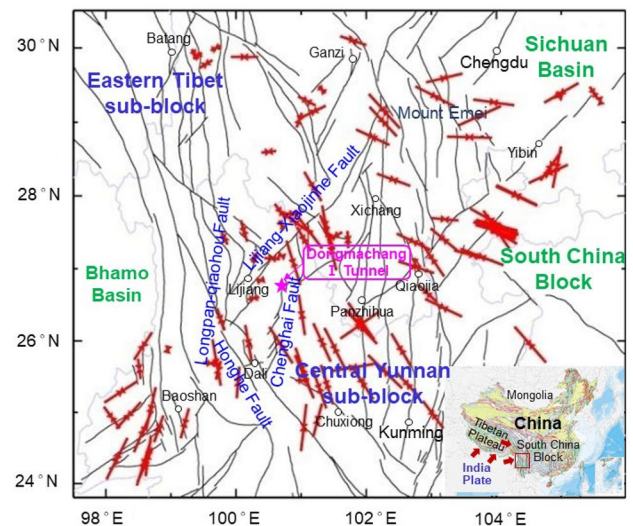


Fig. 2 Regional tectonic and *P*-axis distribution of focal mechanism solution

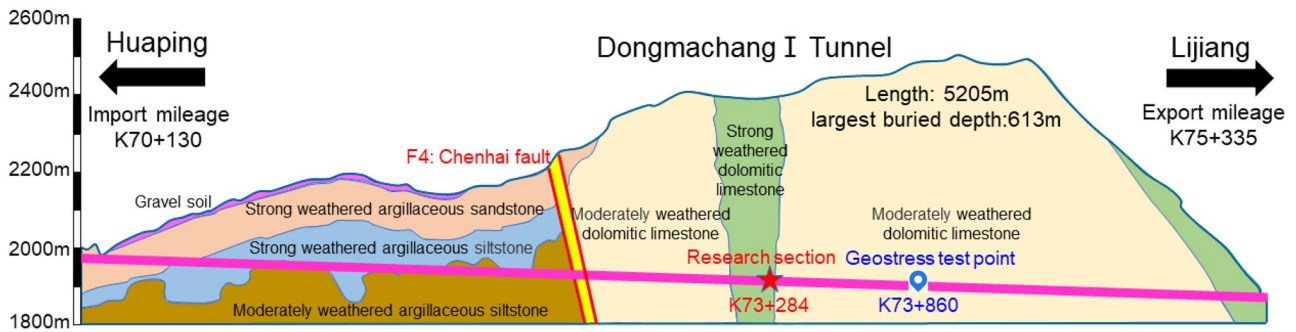


Fig. 3 Longitudinal profile of Dongmachang I tunnel on Huaping-Lijiang highway

Geological environment and engineering background

Regional geological environment

The Dongmachang I tunnel, which is in soft and hard rock inclined contact strata and under high geo-stress, is located on the Huaping-Lijiang highway, Yunnan Province, China (Fig. 1). It is situated in the northwest of the Yunnan-Guizhou Plateau, with a rugged surface and continuous mountains. The geomorphology of the tunnel passage area

is dissolving high-middle mountain and dominated by tectonic denudation and dissolution, karst mountains, which is composed of paleozoic erathem, and carbonate of Devonian system. Moreover, the tunnel passes through the Chenghai fault, which is a Holocene active fault and seismogenic fault, and the angle between the tunnel axis and the fault is 41° (Fig. 1).

The Chenghai fault, located on the geotectonics of the northwestern Yunnan rift zone (Fig. 2), is the most significant active fault on the eastern margin of the Tibetan Plateau, affected by the collision and compression of the Indian

Fig. 4 Features of surrounding rock revealed by tunnel excavation



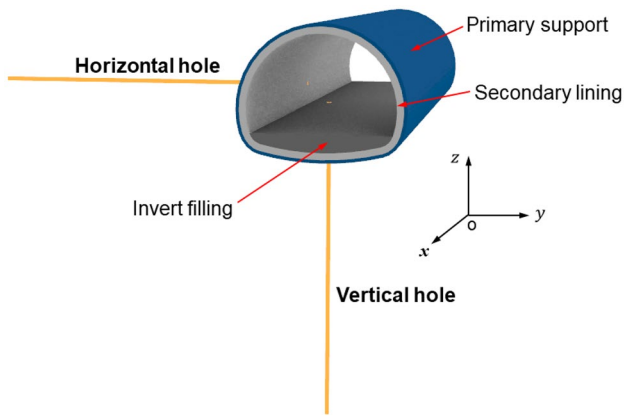


Fig. 5 Layout of in-situ stress test holes

and Eurasian plate (Huang et al. 2021; Luo et al. 2016). In this region, Chenghai fault, Lijiang-Xiaojinhe fault, Lijiang-Jianchuan fault, Longpan-Qiaohou fault, and the northern section of the Honghe fault formed a wedge-shaped block. Driven by the force source, the block moved in the SSW direction.

Chenghai fault is about 95-m wide and 180-km long, with an occurrence of $310^{\circ}\angle 72^{\circ}$. The topography of the fault is clear, along with left-handed dislocations of ridges, water systems, and gullies simultaneously. It controls the distribution of the Late Pleistocene stratum and basins, and the amounts of dislocations are mostly about 200–550 m. According to the trough revealed from four paleo-earthquake events, it is predicted that the repetition time interval of the 7–7.5 magnitude earthquake on the fault is 1500–2000 years. Since the Quaternary, the left-lateral strike-slip movement rate of the Chenghai fault is about 2.0 mm/a. It has a seismogenic capacity of level 7 and impacts the tunnel greatly.

Engineering background

The longitudinal profile of the Dongmachang I tunnel is shown in Fig. 3. The total length of the tunnel is 5205 m, and the largest buried depth is 613 m. The chief strata in the

Table 1 The in-situ stress and direction of rock mass

| Position | Hole depth (m) | Maximum principal stress (MPa) | Minimum principal stress (MPa) | Direction of breaking ($^{\circ}$) |
|-----------------|----------------|--------------------------------|--------------------------------|--------------------------------------|
| Horizontal hole | 34 | 13.12 | 9.78 | 46° |
| Vertical hole | 42.6 | 16.09 | 10.88 | NE75 $^{\circ}$ |

tunnel are the overlying Quaternary Slope Residual layer, the underlying Devonian Middle Tanshanping Formation, and the Lower Jurassic Fengjiahe Formation. Besides, the lithology includes mudstone, argillaceous siltstone, sandstone, quartz sandstone, conglomerate, limestone, and dolomitic limestone, which is obviously different from both sides of the Chenghai fault. The import is mainly Jurassic argillaceous siltstone and mudstone, but the export is primarily Devonian dolomitic limestone and limestone.

Dongmachang I tunnel is a separated two-lane tunnel with a horseshoe-shaped cross-section, 11.5-m wide and 8.55-m high. The tunnel is excavated with three benches, the upper is 9 m, the middle is 12 m, the lower step is 9 m, and the circular excavation footage is 1 m. The rock of the export is mainly the dolomitic limestone (Fig. 4). The rock mass is broken and weak, and the left and right sides are quite different, with an obvious interface. The rock mass on the left side is principally constituted by joints, fissures, and fragments from crushed stones, and the compressive strength is lower than 10 MPa. However, the right side is different, which is moderately weathered, mostly fragmented, and with relatively good lithology.

In-situ stress measurement and calculation

In-situ stress measurement was carried out by hydraulic fracturing. The horizontal and vertical holes were settled in the tunnel export direction K73 + 860 (Fig. 3). The horizontal hole was arranged at the tunnel side wall, and the vertical

Fig. 6 Results of geo-stress measurement

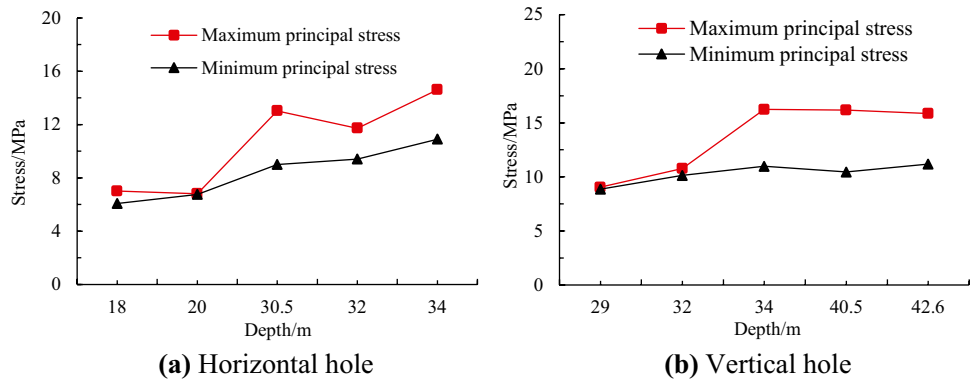
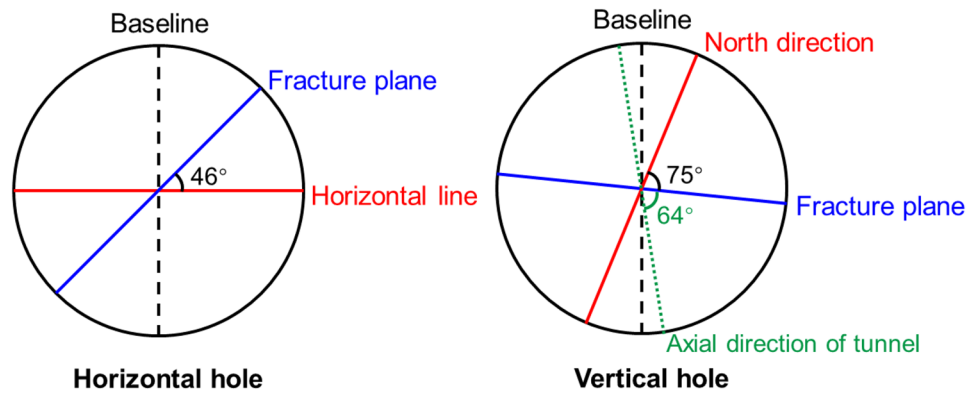


Fig. 7 Results of impression measurement



hole was at the nearby bottom plate (Fig. 5). The horizontal drilling test is used to measure vertical stress and verify the direction of horizontal principal stress. The principal stress values of the different depth of the two test holes are shown in Fig. 6, and the field test results illustrate that the stress increases with the growth of hole depth. The maximum principal stresses for the horizontal and vertical holes are 14.61 MPa and 16.24 MPa, and the minimum are 10.90 MPa and 11.18 MPa, respectively. After the tunnel excavation, the stress on the surrounding rock is redistributed, and the surrounding rock becomes loose and cracked. The tangential stress of surrounding rock firstly increases along with the direction perpendicular to the axis of the tunnel, reaches the maximum at the elastic–plastic boundary of surrounding rock, then gradually decreases, and finally tends to the in-situ stress of rock mass (Luo et al. 2011). Due to the stress release of surrounding rock and the integrity of rock mass, the stress value of the shallow measuring points of each test hole is too low to represent the actual original stress.

Therefore, the mean value of the maximum and minimum principal stresses of three deep points are used as the in-situ stress values of rock mass (Table 1). The maximum in-situ stress of a horizontal hole is 13.12 MPa, and the minimum is 9.78 MPa. After the fracturing of this hole, the maximum principal stress direction impression was measured in this hole by using an automatic orientation instrument, and the fracture direction intersected with the horizontal at 46° (Fig. 7). The maximum in-situ stress of a vertical hole is 16.09 MPa, and the minimum is 10.88 MPa. The fracture direction is 75° north to east, and the included angle with the axial direction of the tunnel is about 64° (Fig. 7).

Generally, there is a certain angle between the principal stress direction of in-situ stress and the axial direction of the tunnel. In-situ stress of tunnel cross-section can be obtained by three-dimensional transformation calculation (Chen et al. 2019a, b; Xu et al. 2018), and the formulas of the xoy plane are as follows:

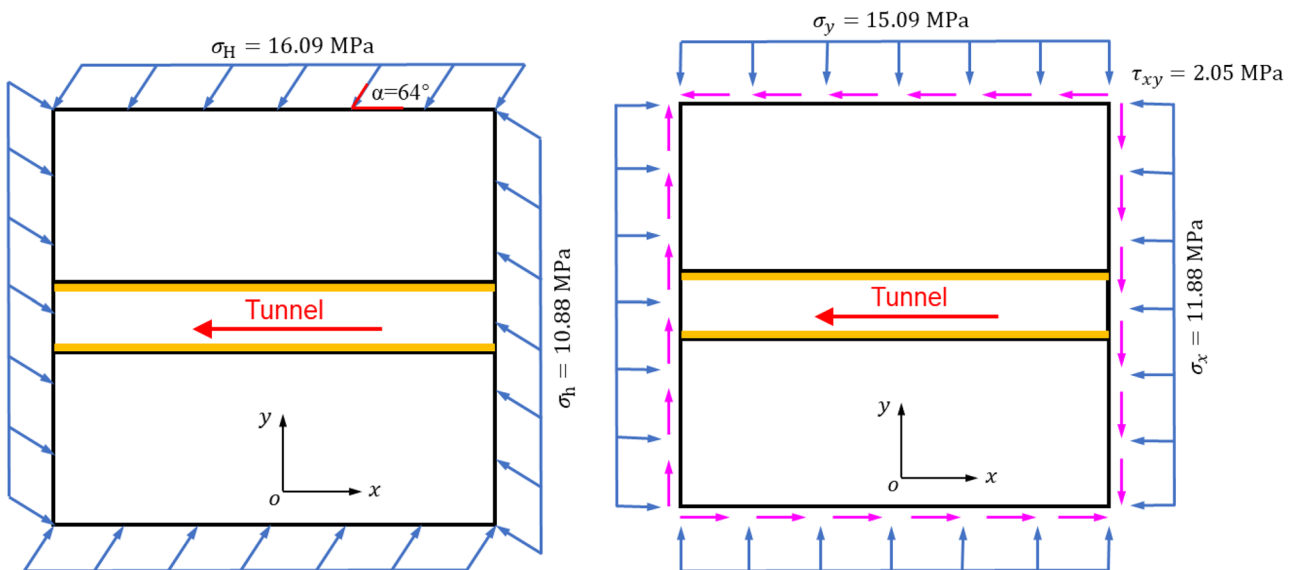


Fig. 8 Distribution of in-situ geo-stress measured by the vertical hole

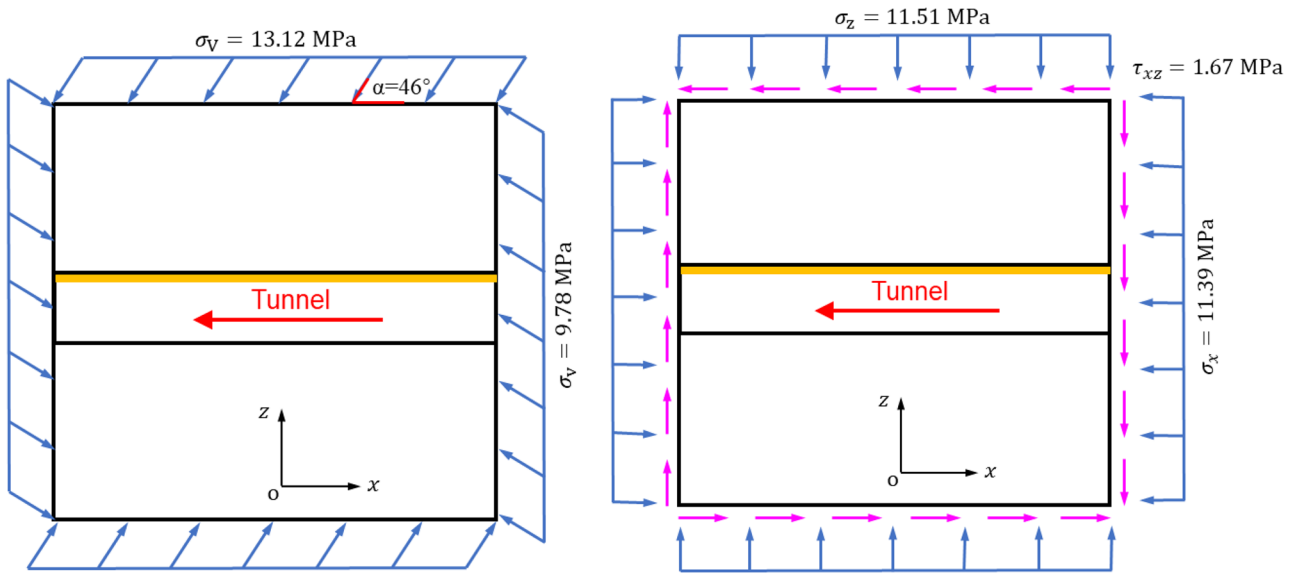


Fig. 9 Distribution of in-situ geo-stress measured by the horizontal hole

$$\sigma_x = \frac{\sigma_H + \sigma_h}{2} + \frac{\sigma_H - \sigma_h}{2} \cos(2\alpha) \tag{1}$$

$$\sigma_y = \frac{\sigma_H + \sigma_h}{2} - \frac{\sigma_H - \sigma_h}{2} \cos(2\alpha) \tag{2}$$

$$\tau_{xy} = \frac{\sigma_H - \sigma_h}{2} \sin(2\alpha) \tag{3}$$

where σ_x and σ_y are the stresses in x and y directions, respectively, τ_{xy} is the tangential stress, σ_H and σ_h are the maximum

and the minimum horizontal principal stresses, respectively, and α is an angle of the maximum principal stress.

The distribution of in-situ geo-stress obtained from the vertical hole is shown in Fig. 8. Similarly, the distribution of in-situ geo-stress obtained from the horizontal hole is described in Fig. 9. It can be seen that σ_x obtained from vertical and horizontal holes are 11.88 MPa and 11.39 MPa, respectively, which are close to each other, showing that the calculation results are accurate. Considering that the stress on the tunnel is a plane strain problem, the tangential stress is ignored. Therefore, the distribution of in-situ geo-stress of tunnel cross-section is obtained, and the tunnel is mainly subjected to horizontal stress (Fig. 10).

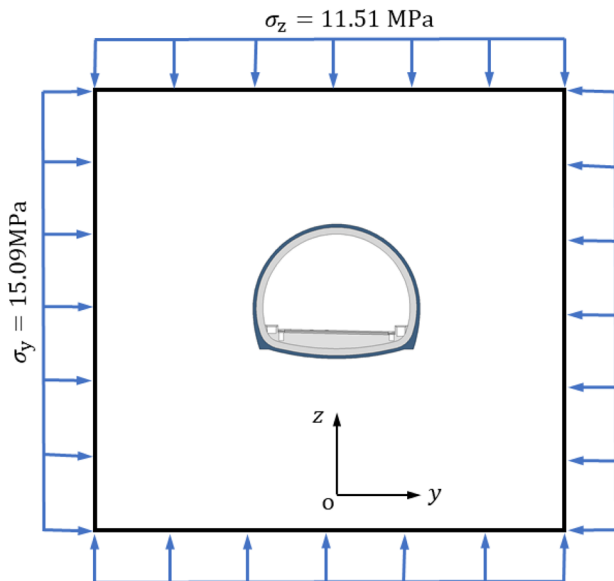


Fig. 10 Distribution of in-situ geo-stress in tunnel cross-section

Asymmetric deformation and mechanical behavior

The characteristics of deformation and failure

The specific excavation method and supporting parameters of the test section are shown in Table 2.

The surrounding rock condition of the tunnel is generally poor, with a strength of less than 10 MPa and a strength-stress ratio (R_c/σ_{max}) less than 2.0. According to China’s Standard Code for Classification of Engineering Rock Mass (Ministry of Water Resources of PRC 2015), it belongs to an extremely high-stress area, and the surrounding rock is prone to squeezing deformation and failure after tunnel excavation. The primary support and secondary lining nearing the soft and hard rock junction section K73 + 284 of the tunnel were seriously deformed and failed (Figs. 11 and 12). There was

Table 2 The excavation method and supporting parameters of the test section

| Test section position | Excavation method | Advance support | Mortar bolt | Steel arch | Primary support | Secondary lining |
|-----------------------|-------------------|---|--------------------------|-------------------------|-----------------|------------------|
| K73 + 284 | Three-bench | 4.5-m long, 0.8-m spacing and overlapping length of 1.3 m | 3-m long and 1-m spacing | I 18 with 0.8-m spacing | 25-cm C25 | 50-cm C30 |

a great difference between the left and right sides of the surrounding rock, which caused asymmetric deformation and failure. It could be obviously seen that the left spandrel of the primary support has squeezing deformation and spalling failure. Shortly after the secondary lining was applied, the left spandrel appeared penetrating cracking, and the temporarily supported steel arch frame also buckled.

The vault settlement and horizontal convergence deformation of the test section were monitored, and the results are shown in Fig. 13. According to the real-time monitoring, with the excavation of the upper, middle, and lower bench, the vault settlement and horizontal convergence increased. The displacement value and rate of vault settlement were much larger than horizontal convergence. The displacement on the left side was obviously larger than on the right side, $G2 > G1 > G3$, with values of 699 mm, 677 mm, and 585 mm, respectively. The lower horizontal convergence value $S2$ was larger than the upper $S1$, and the values were 416 mm and 215 mm individually. In a word, the tunnel was mainly vertical deformation, with a large deformation value and obvious asymmetric deformation characteristics.

In order to understand the asymmetric deformation and failure mechanism of the tunnel in detail, FLAC^{3D} finite difference software was used for numerical simulation analysis and Mohr–Coulomb plastic constitutive model was used. The numerical model was established according

to the actual geological conditions and the tunnel support design. The lithology of the left and right sides of the surrounding rock was quite different. The model was established according to the field investigation (Fig. 4) and is shown in Fig. 14. In order to reduce the boundary effect, the model size was about three times the tunnel diameter, and the length, width, and height were 80 m, 50 m, and 80 m, respectively. The fixed boundary was adopted at the bottom of the model, and the measured results of geostress were employed at other boundaries. The top of the model was loaded with 11.51 MPa, and the left and right sides were 15.09 MPa (Fig. 10). The before and after of the model were 11.64 MPa, which was the average stress in the x -direction in Figs. 8 and 9.

According to the field investigation, geological survey data, and tunnel design documents, the physical and mechanical parameters of the left and right surrounding rocks are shown in Table 3. Parameters of tunnel supporting structure are shown in Tables 4 and 5. The elastic modulus of primary support is considered by the equivalent of the steel arch and shotcrete, and the formula is as follows:

$$E_s A_s + E_c A_c = E_e A_e \tag{4}$$

where E_s and E_c are the elastic modulus of the steel and shotcrete, A_s and A_c are the areas of the steel and shotcrete,

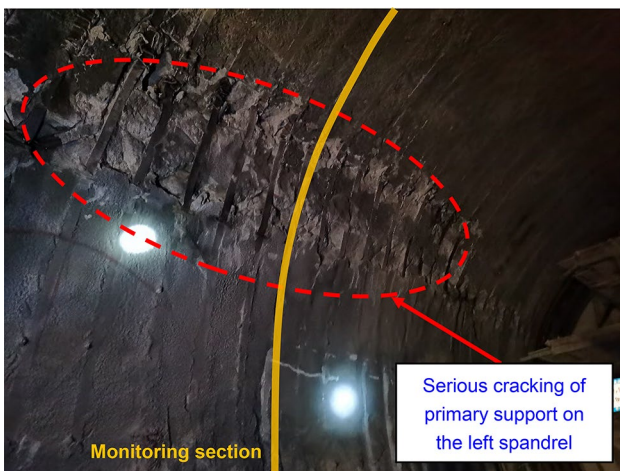


Fig. 11 Deformation and failure characteristics of primary support

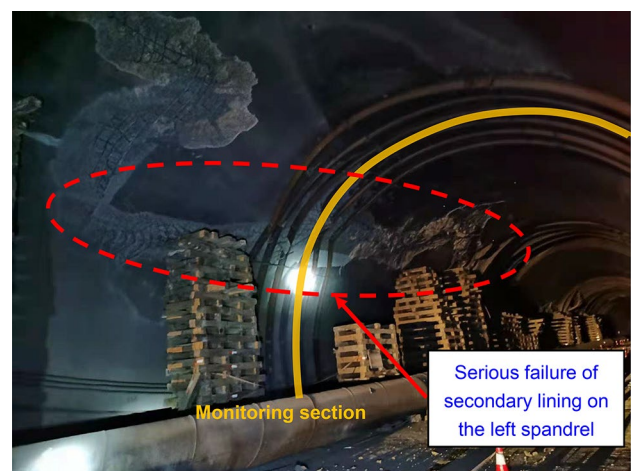


Fig. 12 Failure characteristics of secondary lining

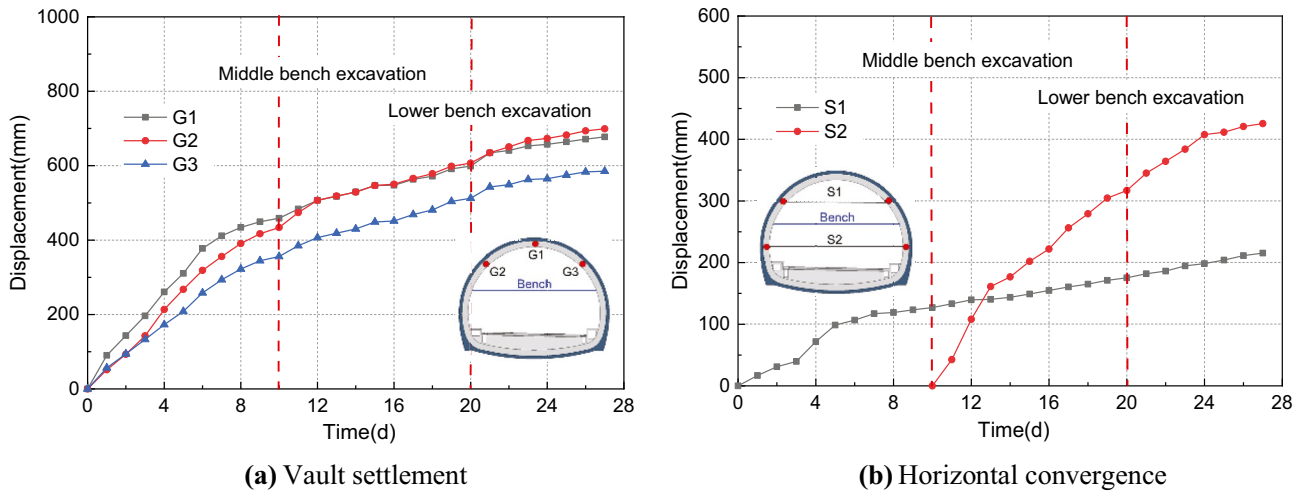


Fig. 13 Monitoring results of surrounding rock deformation

and E_c is the equivalent elastic modulus of steel arch and shotcrete.

From the simulated displacement contours (Fig. 15a), it was clearly seen that the vertical displacement of the vault deflected to the left after tunnel excavation, and the displacement of the arch bottom reached the maximum on the left side of the interface between soft and hard rock. The maximum displacement of vault settlement was 712 mm on the left side of the vault, and the arch bottom uplift was 402 mm at the arch foot. Figure 15b showed the horizontal displacement after tunnel excavation, and the displacement on the left side was obviously larger than that on the right side. The maximum horizontal displacement was 598 mm on the left side near spandrel to hance and was 321 mm on the right side at spandrel from hard rock to soft rock, which showed that the tunnel had obvious asymmetric deformation when crossing the inclined contact section of soft and hard rock.

The real field monitoring started after the tunnel excavation. Therefore, by subtracting the displacement before excavation from the simulated displacement data, the vault

settlement and horizontal convergence deformation consistent with the actual situation could be obtained (Fig. 16). It also showed that the vault displacement deflected to the left with the excavation of the tunnel. The displacement G1 was larger than G2 just after the upper bench excavation, and G2 was gradually larger than G1 after the middle bench excavation. The overall settlement of the vault was $G2 > G1 > G3$. Furthermore, the displacements of G1, G2, and G3 were 597 mm, 634 mm, and 521 mm, respectively, which were close to the measured values. The lower horizontal convergence value S2 was larger than the upper S1, and the values were 437 mm and 259 mm individually, which were also close to the monitored data.

The displacement of the numerical simulation was consistent with the trend of the field monitoring (Fig. 17). In detail, the settlement displacement of the vault was larger than horizontal convergence, and the settlement on the left side was greater than that on the right side, which was about 1.2 times. Clearly, it showed that the numerical simulation in this paper could reflect the actual situation on site.

Fig. 14 Numerical calculation model

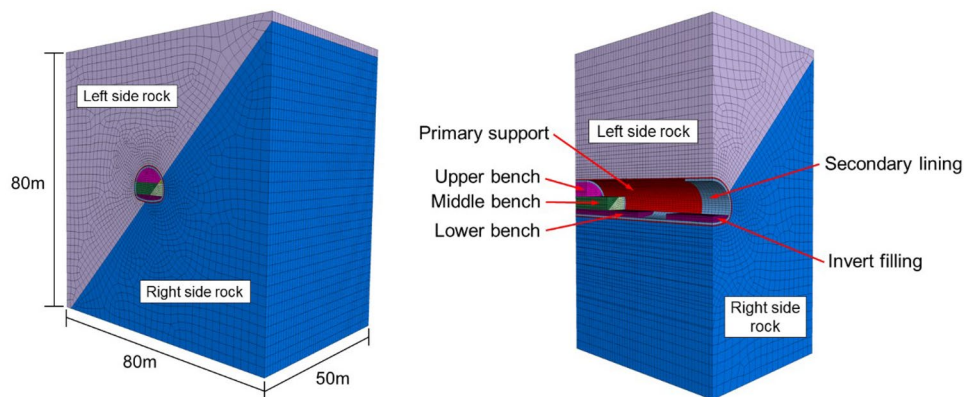


Table 3 Physical and mechanical parameters of rock mass

| Surrounding rock | Elastic modulus (GPa) | Poisson | Density (kg/m ³) | Cohesion (kPa) | Internal friction angle (°) | Tensile strength (MPa) |
|------------------|-----------------------|---------|------------------------------|----------------|-----------------------------|------------------------|
| Left side rock | 1.0 | 0.37 | 2380 | 70 | 27 | 0.6 |
| Right side rock | 3.0 | 0.30 | 2400 | 300 | 35 | 2.5 |

Mechanical behavior

After tunnel excavation, the vibrating wire sensors were embedded to monitor the internal stress of the steel arch, the pressure between primary support and surrounding rock, and the internal stress of the secondary lining. The main sensors were concrete strain gauge, stress gauge, and pressure cell, with measuring ranges of 60 MPa, 300 MPa, and 2 MPa, respectively. The layout of monitoring components in the test section is depicted in Fig. 18.

According to the monitoring results of surrounding rock pressure in Fig. 19, the surrounding rock pressure extremely and continuously increased in the beginning and then gradually slowed down. The secondary lining was applied on the 42nd day, and the pressure at the left spandrel increased rapidly on the 92nd day. On the 105th day, the secondary lining of the left spandrel was cracked, and other parts were not damaged. The maximum pressure of the surrounding rock reached 2140 kPa at the left spandrel, and the pressures of the vault, left hance, right spandrel, and right hance were 793 kPa, 612 kPa, 569 kPa, and 382 kPa, respectively. The internal stress of the steel arch was in the state of compression, and it also showed the same change rule (Fig. 20). Although the secondary lining was applied, the pressure reached 348 MPa, exceeded the measuring range of the stress gauge (300 MPa), and failed to read. The stresses of the vault, left hance, right spandrel, and right hance were 272 MPa, 254 MPa, 201 MPa, and 60 MPa, separately.

The results of stress monitoring of primary support showed that the stress at the left spandrel and vault increased rapidly before the secondary lining was applied, while the stresses at other parts increased slowly (Fig. 21). After the secondary lining was installed, the stress on the primary supporting structure was controlled, but the compressive stress at the left spandrel was 50 MPa, which has exceeded the ultimate compressive strength of C25 concrete. The maximum compressive stress at the vault also reached 41 MPa,

which decreased to 28 MPa due to stress release after cracking of the secondary lining. The stresses of left hance, right spandrel, and right hance were 16 MPa, 9 MPa, and 7 MPa, correspondingly, which did not exceed the ultimate compressive strength of the concrete and had not been damaged. After the secondary lining was applied, it became the main bearing body and shared the stress of the primary support so that the stress of the primary support no longer increased (Fig. 21), but the stress of the secondary lining continued to increase (Fig. 22). On the 60th day after the secondary lining was used, the left spandrel cracked and the stress at this point reached to 42 MPa, which exceeded the ultimate compressive strength of C30 concrete. Besides, the stresses at the vault, left hance, right spandrel, and right hance were respectively 20 MPa, 14 MPa, 13 MPa, and 9 MPa. After the secondary lining cracked, the stress in the left spandrel and vault increased rapidly, but the stress for other parts arose slowly. On the 85th day, the structure failed and the steel arch frame was used for temporary support. At this time, the stresses of the vault, left spandrel, left hance, right spandrel, and right hance were 32 MPa, 62 MPa, 19 MPa, 18 MPa, and 11 MPa, separately. Therefore, we speculated that the stress was mainly borne by the temporary steel arch, and the stress of the secondary lining gradually decreased. The stress value and change process of the measuring points for the supporting structure could be clearly obtained from the monitoring. The results showed that the stress at the left spandrel was the largest and the damage had occurred, which was consistent with the actual damage position on site.

Simulated stress contours of primary support and secondary lining are shown in Fig. 23. The maximum stress occurred at the left spandrel, reaching 48.8 MPa, exceeding the ultimate compressive strength of C30 concrete, which was consistent with the failure position on site. The stresses of primary support at the vault, left spandrel, right spandrel, left hance, and right hance were 21.2 MPa,

Table 4 Parameters of bolt and advanced pipes

| Structure name | Diameter (mm) | Length (cm) | Spacing (cm) | Density (kg/m ³) | Elastic modulus (GPa) |
|----------------|---------------|-------------|--------------|------------------------------|-----------------------|
| Bolt | 25 | 300 | 100 | 7850 | 210 |
| Advanced pipes | 42 | 450 | 80 | 7850 | 210 |

Table 5 Parameters of concrete

| Structure name | Thickness (cm) | Density (kg/m ³) | Elastic modulus (GPa) | Poisson's ratio |
|------------------|----------------|------------------------------|-----------------------|-----------------|
| Primary support | 25 | 2400 | 32.05 | 0.20 |
| Secondary lining | 50 | 2500 | 31.50 | 0.20 |

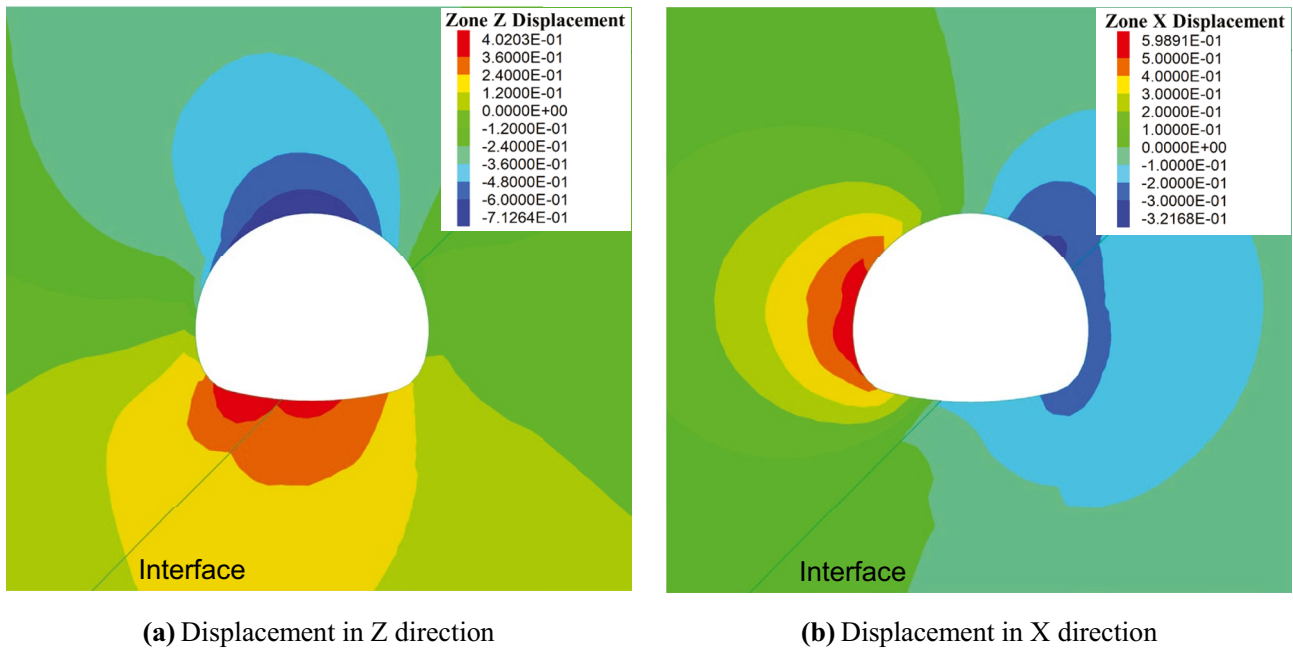


Fig. 15 Simulated displacement contours of the surrounding rock

45.3 MPa, 17.0 MPa, 25.8 MPa, and 10.1 MPa, and the stresses of secondary lining were 19.1 MPa, 40.7 MPa, 21.3 MPa, 28.5 MPa, and 9.9 MPa, respectively, which was consistent with the law of field measured stress. The comparison result between measured and simulated stress before secondary lining cracking is presented in Fig. 24. The stress of the left spandrel was the largest, and vault, left hance, right spandrel, and right hance were smaller. Obviously, this bias phenomenon was associated with the inclined contact between soft and hard rocks under high geo-stress.

We extracted the stress data of the secondary lining and calculated the axial force and bending moment (Fig. 25a and b). The axial force and bending moment at the spandrel were the largest, reaching 12 675.0 kN and 997.1 kN·m, respectively. The corresponding safety factor of the lining could be calculated based on the axial force and the bending moment, which was used to visually evaluate the safety of the lining structure. We applied the method recommended in the Design Specification for Highway Tunnels to calculate the safety factor of the secondary lining (Chen et al. 2020b). The minimum value at the left

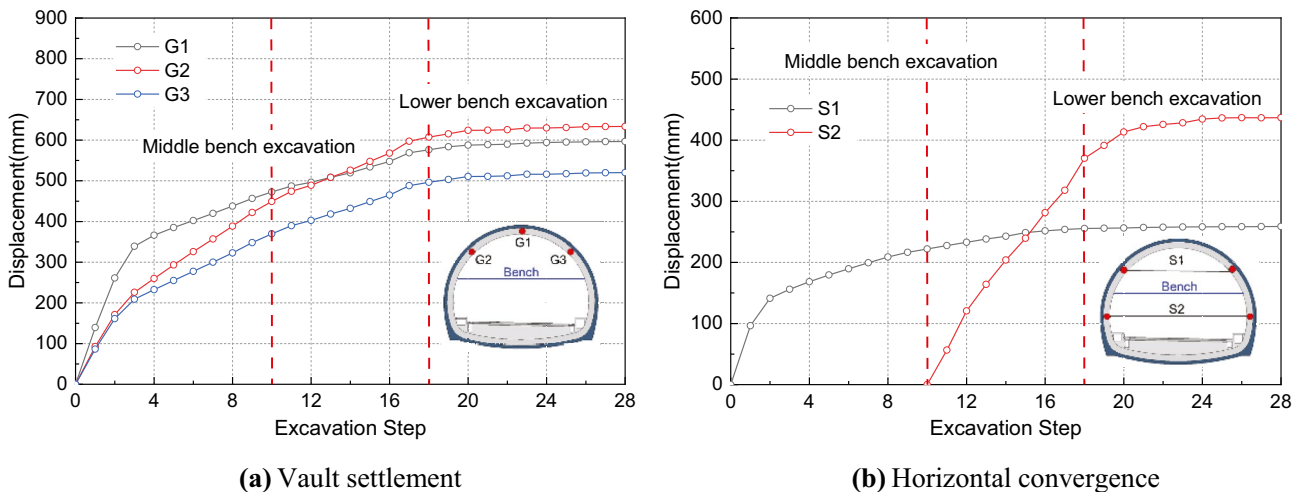


Fig. 16 Simulated displacements of the surrounding rock

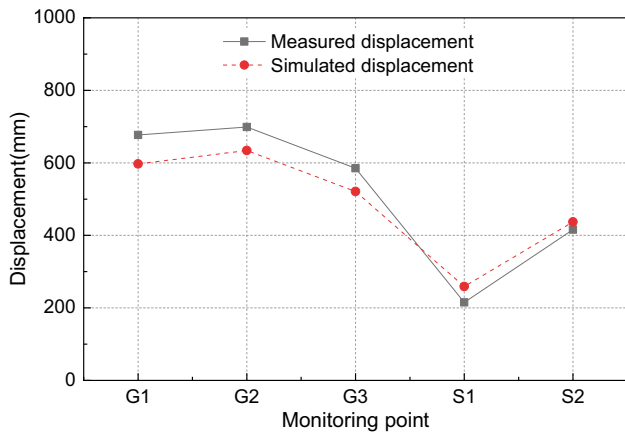
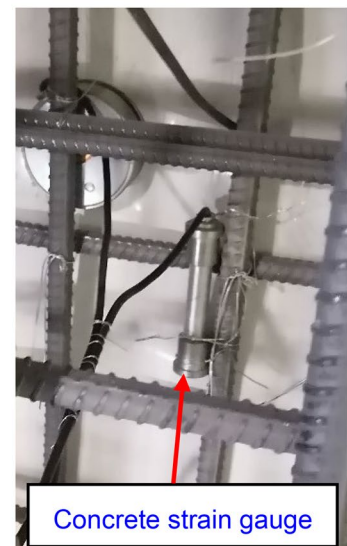
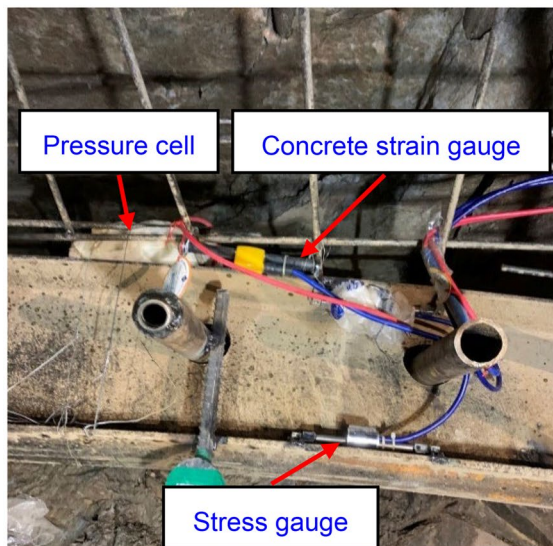
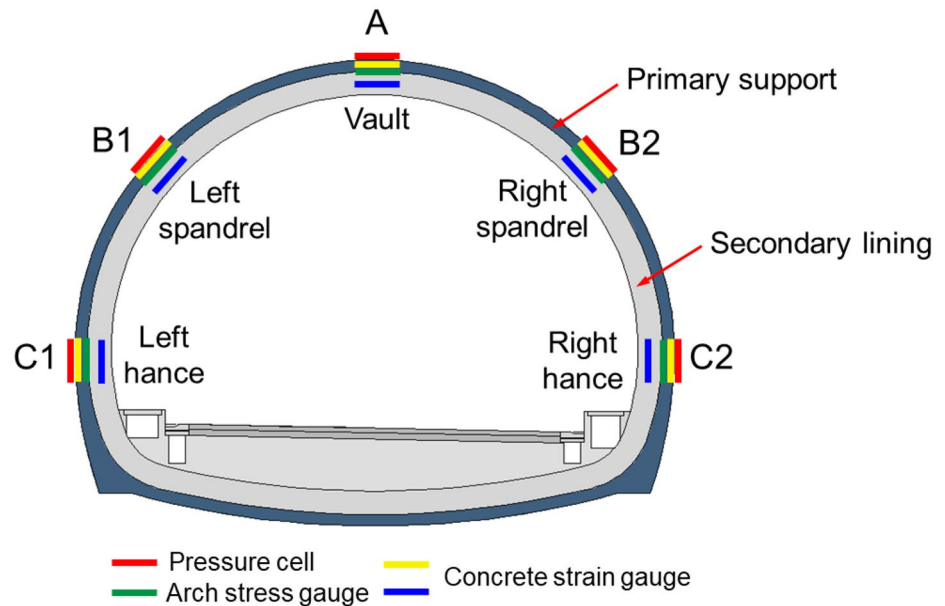


Fig. 17 Comparison of measured and simulated displacement

spandrel was 0.7, which was less than 1.0, and it was in a state of failure (Fig. 25c). Near the spandrel and the hance, the safety factor was also close to 1.0, which was in a critical failure state. However, the safety factors of other parts, which were in a stable state, met the design requirements.

Under high geo-stress, the excavation of soft-hard rock tunnel with inclined contact is often accompanied by asymmetric deformation. The deformation and stress on the side of the soft rock are large, and the maximum occurs in the normal direction of the interface between soft and hard rock. When the supporting structure cannot work, damage often occurs here. Therefore, it is suggested to strengthen the supporting measures of the soft side when encountering such surrounding rock, such as applying long bolts on the side of bias to reinforce and control in advance.

Fig. 18 Layout of monitoring components in the test section



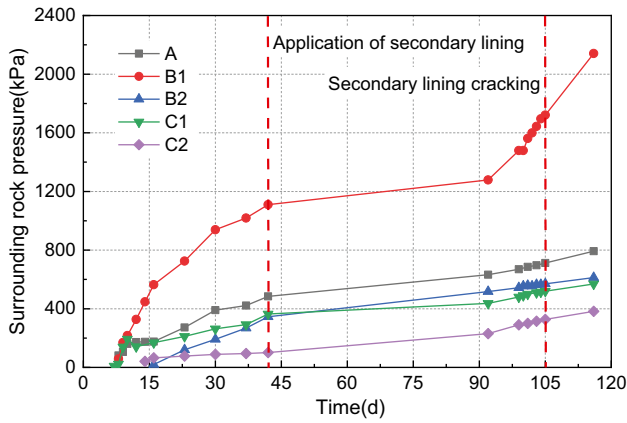


Fig. 19 Monitoring value of surrounding rock pressure

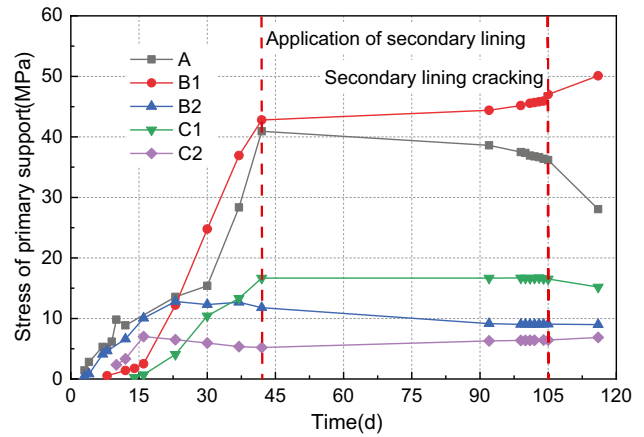


Fig. 21 Stress monitoring value of primary support

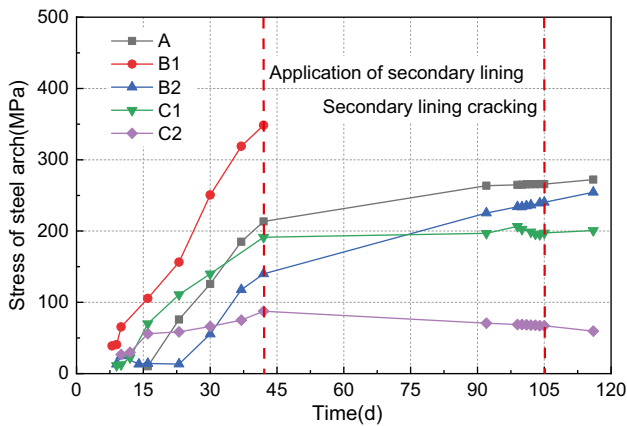


Fig. 20 Stress monitoring value of steel arch

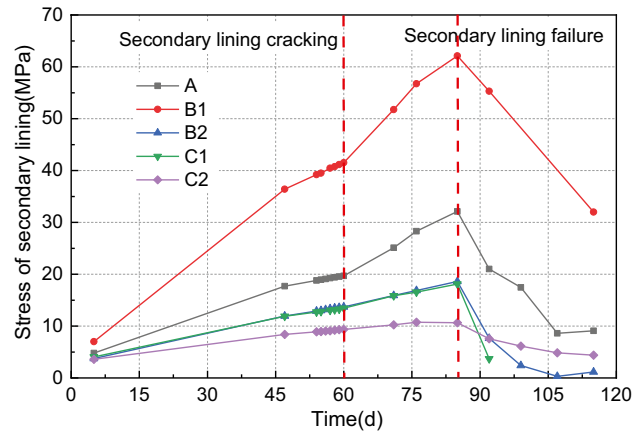
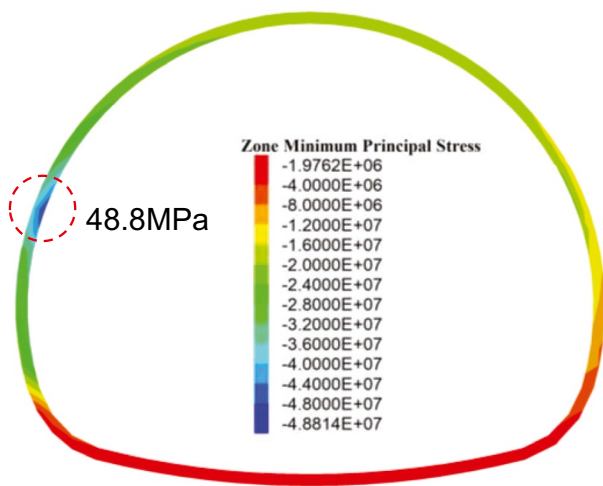
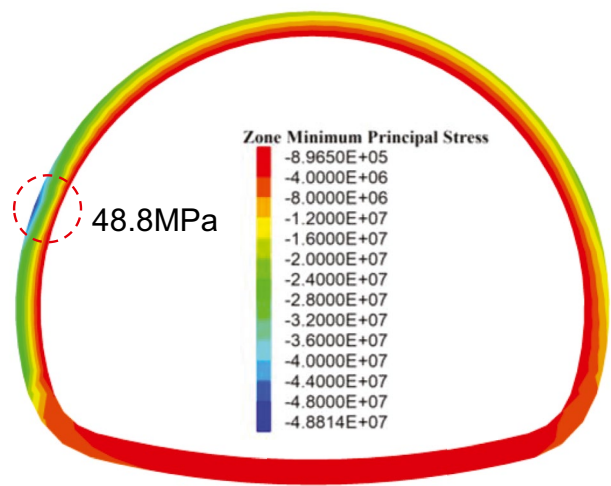


Fig. 22 Stress monitoring value of secondary support



(a) Stress of primary support



(b) Stress of secondary lining

Fig. 23 Simulated stress contours of primary support and secondary lining

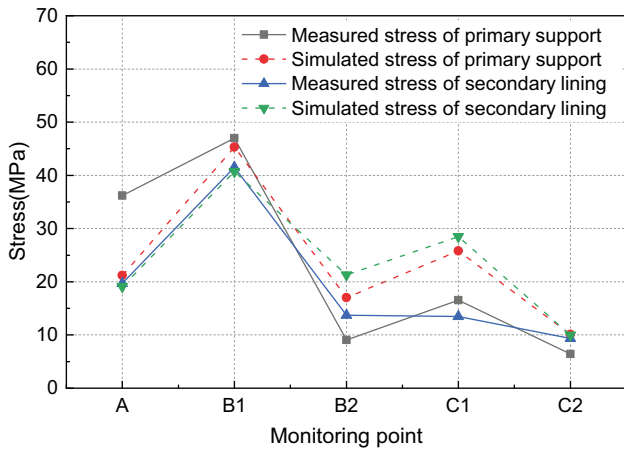


Fig. 24 Comparison of measured and simulated displacement

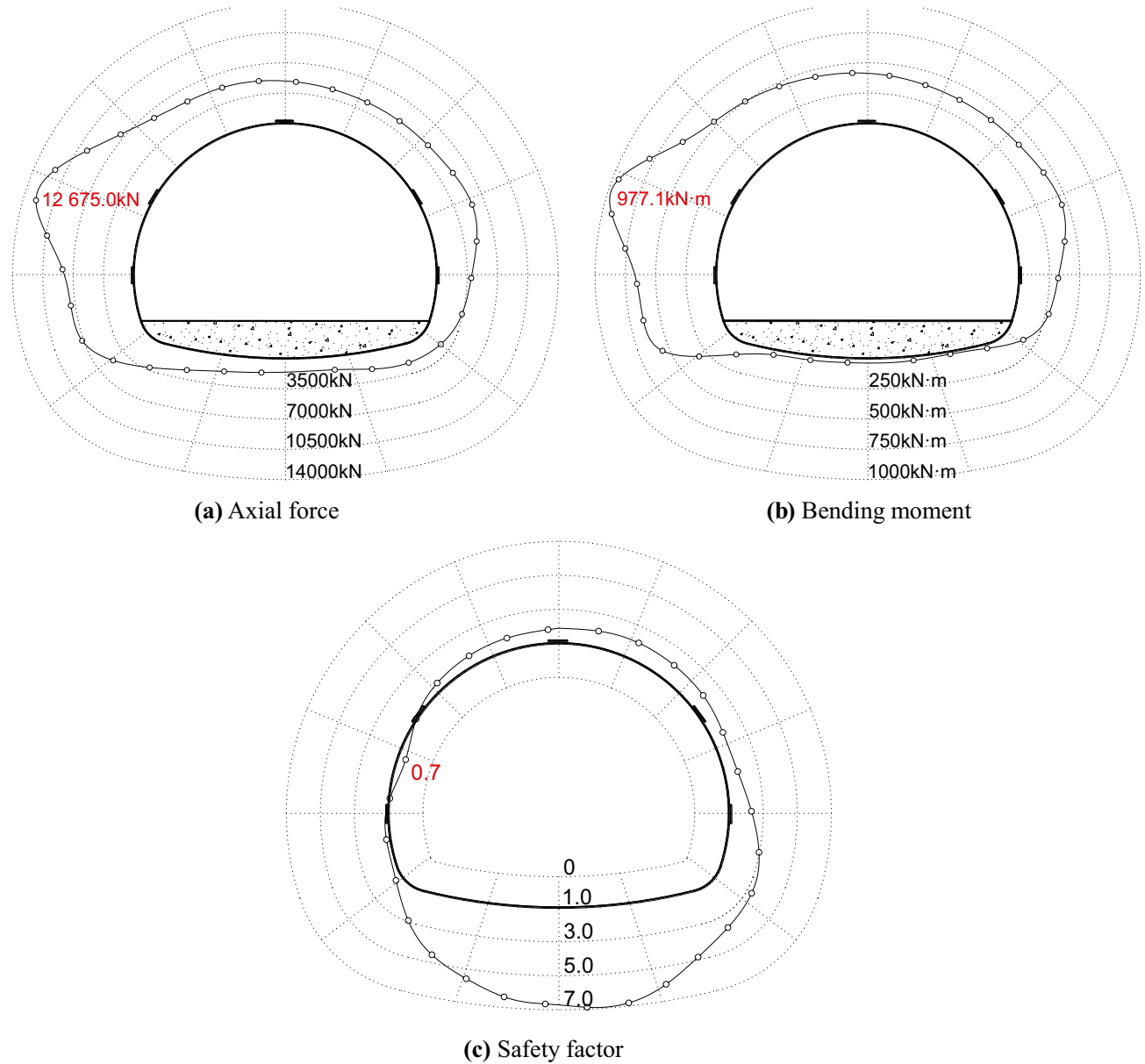


Fig. 25 Mechanical behavior of secondary lining

Conclusions

This paper describes a case study of asymmetric deformation of soft and hard inclined contact of dolomitic limestone and the unequal pressure behavior of supporting structure in Dongmachang I tunnel in Yunnan Province, China. Based on the field measurements of supporting structure and numerical simulation, the asymmetric deformation characteristics and mechanical behavior in soft-hard rock inclined contact strata are analyzed. Based on the results of this study, the major conclusions are as follows.

- (1) Through in-situ stress test and calculation, it is concluded that the stress was mainly in the horizontal direction. The horizontal stress of the tunnel is 15.09 MPa, the direction is 75° from north to east, the included angle with the tunnel axis is about 64°, and the vertical stress is 11.51 MPa. The tunnel is extremely in high geo-stress.
- (2) The large deformation disaster of the surrounding rock and the damage to the secondary lining in Dongmachang I tunnel at the Chenghai active fault zone were caused by high geo-stress and dolomitic broken limestone. Affected by horizontal tectonic stress and inclined contact between soft and hard rocks, the maximum squeezing deformation and pressure occurred at the left spandrel of the tunnel.
- (3) According to the results of field monitoring and numerical simulation, we find that the settlement displacement of the vault is larger than horizontal convergence and the settlement displacement on the left side is about 1.2 times that on the right. Besides, the left spandrel of surrounding rock pressure is about 3.5 times that on the right. On average, the stress of the left spandrel of the primary support and secondary lining is about 3.3 times that of the right. The asymmetric deformation and stress characteristics for tunnels in soft-hard inclined contact strata are revealed.
- (4) Based on numerical simulation calculations, the minimum safety factor at the left spandrel is only 0.7, which clearly shows that the secondary lining is in a failed state. This is consistent with the actual damage result in the field, which vividly represents the failure of the secondary lining under bias pressure on site.

Acknowledgements This study was supported by the High Speed Railway and Natural Science United Foundation of China (Grant No. U1734205) and the CSCEC technology R & D plan of China (No. CSCEC-2021-Z-26). The study in Dongmachang I Tunnel was permitted by Yunnan Huali Expressway Investment Development Co., Ltd, which is the responsible authority for this project.

References

- Bai JW, Feng GR, Wang ZH et al (2019) Experimental investigations on the progressive failure characteristics of a sandwiched coal-rock system under uniaxial compression. *Appl Sci-Basel* 9. <https://doi.org/10.3390/app9061195>
- Cao CY, Shi CH, Lei MF et al (2018) Squeezing failure of tunnels: a case study. *Tunn Undergr Space Technol* 77:188–203. <https://doi.org/10.1016/j.tust.2018.04.007>
- Chen JX, Liu WW, Chen LJ et al (2020a) Failure mechanisms and modes of tunnels in monoclinic and soft-hard interbedded rocks: a case study. *KSCE J Civ Eng* 24:1357–1373. <https://doi.org/10.1007/s12205-020-1324-3>
- Chen ZQ, He C, Xu GW et al (2019a) A case study on the asymmetric deformation characteristics and mechanical behavior of deep-buried tunnel in phyllite. *Rock Mech Rock Eng* 52:4527–4545. <https://doi.org/10.1007/s00603-019-01836-2>
- Chen ZQ, He C, Xu GW et al (2019b) Supporting mechanism and mechanical behavior of a double primary support method for tunnels in broken phyllite under high geo-stress: a case study. *Bull Eng Geol Environ* 78:5253–5267. <https://doi.org/10.1007/s10064-019-01479-1>
- Chen ZQ, He C, Yang WB et al (2020b) Impacts of geological conditions on instability causes and mechanical behavior of large-scale tunnels: a case study from the Sichuan-Tibet highway, China. *Bull Eng Geol Environ* 79:3667–3688. <https://doi.org/10.1007/s10064-020-01796-w>
- Ding JW, Zhang S, Zhang H et al (2021) Ground settlement caused by shield tunneling in soil-rock composite strata. *J Perform Constr Fac* 35. [https://doi.org/10.1061/\(asce\)cf.1943-5509.0001631](https://doi.org/10.1061/(asce)cf.1943-5509.0001631)
- Feng WK, Huang RQ, Li TB (2012) Deformation analysis of a soft-hard rock contact zone surrounding a tunnel. *Tunn Undergr Space Technol* 32:190–197. <https://doi.org/10.1016/j.tust.2012.06.011>
- Huang X, Wu Z, Liu F et al (2021) Tectonic interpretation of the main paleoseismic landslides and their distribution characteristics in the Chenghai Fault Zone, Northwest Yunnan. *Earth Sci Front* 28:125–139 (in Chinese)
- Liu WW, Chen JX, Chen LJ et al (2021) Deformation evolution and failure mechanism of monoclinic and soft-hard interbedded strata: study of Muzhailing tunnel. *J Perform Constr Fac* 35. [https://doi.org/10.1061/\(asce\)cf.1943-5509.0001605](https://doi.org/10.1061/(asce)cf.1943-5509.0001605)
- Luo CW, Li HB, Liu YQ (2011) Characteristics of in-situ stress and variation law of plastic zone of surrounding rocks around deep tunnels in a coal mine. *Chin J Rock Mech Eng* 30:1613–1618 (in Chinese)
- Luo J, Zhao CP, Lu J et al (2016) Characteristics of focal mechanisms and the stress field in the southeastern margin of the Tibetan Plateau. *Pure Appl Geophys* 173:2687–2710. <https://doi.org/10.1007/s00024-016-1350-8>
- Meng LB, Li TB, Jiang Y et al (2013) Characteristics and mechanisms of large deformation in the Zhegu mountain tunnel on the Sichuan-Tibet highway. *Tunn Undergr Space Technol* 37:157–164. <https://doi.org/10.1016/j.tust.2013.03.009>
- Ministry of Water Resources of PRC (2015) Standard for engineering classification of rock mass. China Planning Press, Beijing, GB/T, pp 50218–52014
- Shi LK, Zhou H, Song M et al (2021) Geomechanical model test for analysis of surrounding rock behaviours in composite strata. *J Rock Mech Geotech* 13:774–786. <https://doi.org/10.1016/j.jrmge.2020.12.002>
- Sun XM, Zhao CW, Tao ZG et al (2021) Failure mechanism and control technology of large deformation for muzhailing tunnel in stratified rock masses. *Bull Eng Geol Environ* 80:4731–4750. <https://doi.org/10.1007/s10064-021-02222-5>
- Tao ZG, Cao JD, Yang L et al (2020) Study on deformation mechanism and support measures of soft surrounding rock in muzhailing deep tunnel. *Adv Civ Eng* 2020. <https://doi.org/10.1155/2020/9367916>

- Wang W, Hu MJ, Zhang HW et al (2019) Conversion timing of tunnel excavation methods in upper-soft and lower-hard stratum based on displacement direction angle theory: case study. *Int J Geomech* 19. [https://doi.org/10.1061/\(asce\)gm.1943-5622.0001380](https://doi.org/10.1061/(asce)gm.1943-5622.0001380)
- Wu B, Huang W (2020) Uniaxial compression mechanical properties of rock samples in soft and hard composite strata. *Adv Mater Sci Eng* 2020. <https://doi.org/10.1155/2020/5920348>
- Xu GW, He C, Chen ZQ et al (2020) Transversely isotropic creep behavior of phyllite and its influence on the long-term safety of the secondary lining of tunnels. *Eng Geol* 278. <https://doi.org/10.1016/j.enggeo.2020.105834>
- Xu GW, He CA, Chen ZQ et al (2018) Transverse isotropy of phyllite under Brazilian tests: laboratory testing and numerical simulations. *Rock Mech Rock Eng* 51:1111–1135. <https://doi.org/10.1007/s00603-017-1393-x>
- Yang L, Gao F, Wang X et al (2019a) Energy evolution law and failure mechanism of coal-rock combined specimen. *J China Coal Soc* 44:3894–3902
- Yang SQ, Chen M, Fang G et al (2018) Physical experiment and numerical modelling of tunnel excavation in slanted upper-soft and lower-hard strata. *Tunn Undergr Space Technol* 82:248–264. <https://doi.org/10.1016/j.tust.2018.08.049>
- Yang SQ, Tao Y, Xu P et al (2019b) Large-scale model experiment and numerical simulation on convergence deformation of tunnel excavating in composite strata. *Tunn Undergr Space Technol* 94. <https://doi.org/10.1016/j.tust.2019.103133>
- Yang WB, Jiang YJ, Gu XX et al (2021) Deformation mechanism and mechanical behavior of tunnel within contact zone: a case study. *Bull Eng Geol Environ* 80:5657–5673. <https://doi.org/10.1007/s10064-021-02255-w>
- Zhang J, Liang Y, Feng TG (2020) Investigation of the cause of shield-driven tunnel instability in soil with a soft upper layer and hard lower layer. *Eng Fail Anal* 118. <https://doi.org/10.1016/j.engfailanal.2020.104832>